A Multi-Objective Flight Control Approach for Performance Adaptive Aeroelastic Wing

Nhan Nguyen*
NASA Ames Research Center, Moffett Field, CA 94035
Ezra Tal †
Delft University of Technology, Delft, 2629 HS, Netherlands

As aircraft wings become much more flexible due to the use of light-weight composites material, adverse aerodynamics at off-design performance can result from changes in wing shapes due to aeroelastic deflections. Increased drag, hence more fuel burn, is a potential consequence. Without means for aeroelastic compensation, the benefit of weight reduction from the use of light-weight material could be negated by less optimal aerodynamic performance at off-design. Performance Adaptive Aeroelastic Wing (PAAW) technology can potentially address these technical challenges for future flexible wing transports. PAAW technology leverages multi-disciplinary solutions to maximize the aerodynamic performance payoff of future adaptive wing design, while addressing simultaneously operational constraints that can prevent the aerodynamic performance from being realized. These operational constraints include reduced aeroelastic stability margins, increased airframe responses to gust and maneuver loads, pilot handling qualities, and ride qualities. All of these constraints while seeking the maximum aerodynamic performance present themselves as a multi-objective flight control solution. The paper presents a multi-objective flight control approach based on a drag-cognizant optimal control method. A concept of virtual control, which was previously introduced, is implemented to address the pair-wise flap motion constraints imposed by the elastomer material. This method is shown to be able to satisfy the constraints. Real-time drag minimization control is considered to be an important consideration for PAAW technology. Drag minimization control has many technical challenges such as sensing and control. An initial outline of a real-time drag minimization control is proposed and will be further investigated in the future. A simulation study of a multi-objective flight control for a flight path angle command with aeroelastic mode suppression and drag minimization demonstrates the effectiveness of the proposed solution.

I. Introduction

Air vehicles are typically designed to maintain sufficient structural rigidity for safe load-carrying capacity. Modern engineered materials such as composites have begun to appear in new airframe designs that can provide less structural rigidity while maintaining the same load-carrying capacity. An example of light-weight airframe design is the Boeing 787 Dreamliner aircraft, which has more flexible wing structures than older-generation aircraft. There is a realization that future air vehicle concepts can be developed to take advantage of the structural flexibility afforded by modern engineered materials to improve aerodynamic efficiency.

As aircraft wings become much more flexible due to the use of light-weight composites material, adverse aerodynamics at off-design performance can result from changes in wing shapes due to aeroelastic deflections. Increased drag, hence more fuel burn, is one such potential consequence. Without means for aeroelastic compensation, the benefit of weight reduction from the use of light-weight material could be negated by less optimal aerodynamic performance at off-design. Performance Adaptive Aeroelastic Wing (PAAW) technology can potentially address these technical challenges for future flexible wing transports. PAAW technology leverages multi-disciplinary solutions to maximize the aerodynamic performance payoff of future adaptive wing design, while addressing simultaneously operational constraints that can prevent the aerodynamic performance from being realized. These operational constraints include reduced aeroelastic stability margins, increased airframe responses to gust and maneuver loads, and degraded pilot handling qualities as well as ride qualities. All of these constraints while seeking the maximum aerodynamic performance present themselves as a multi-objective flight control solution.

*Senior Research Scientist, Associate Fellow AIAA, Intelligent Systems Division, nhan.t.nguyen@nasa.gov, (650)604-4063
†Graduate Student, Faculty of Aerospace Engineering, e.a.tal@student.tudelft.nl, AIAA Student Member

A multi-objective flight control framework will attempt to address these operational constraints and the efficiency goal simultaneously in order to arrive at optimal solutions that can provide good compromise between the efficiency goal and operational constraints. These optimal solutions will be developed for the Variable Camber Continuous Trailing Edge Flap (VCCTEF) concept in this study. The VCCTEF is a possible candidate PAAW concept that is being jointly developed by NASA and Boeing Research & Technology under NASA Advanced Air Transport Technology (AATT) project.

The VCCTEF concept was originally developed by a NASA Innovation Fund study entitled "Elastically Shaped Future Air Vehicle Concept" in 2010.[1,13] This study examined new concepts that can enable active control of wing aeroelasticity to achieve drag reduction. The results showed that a highly flexible wing could be elastically shaped in-flight by active control of wing twist and vertical deflection in order to optimize the local angles of attack to improve aerodynamic efficiency through drag reduction during cruise and enhanced lift performance during take-off and landing. The VCCTEF concept was developed to address this need[1] by providing spanwise load tailoring via a continuous trailing edge whereby the spanwise flap sections are joined together by an elastomer transition material as shown in Fig. 1, and chordwise pressure shaping via a variable camber flap having three chordwise segments as shown in Fig. 2. Initial study results indicate that, for some applications, the VCCTEF system may offer a potential pay-off in drag reduction that could provide significant fuel savings. In order to realize the potential benefit of drag reduction by active span-load and aeroelastic wing shaping control while meeting all other performance requirements and operational constraints, an integrated multi-disciplinary approach must be developed to realize the integrated system benefits of PAAW technology. Figure 1 illustrates the VCCTEF concept installed on a flexible wing GTM.

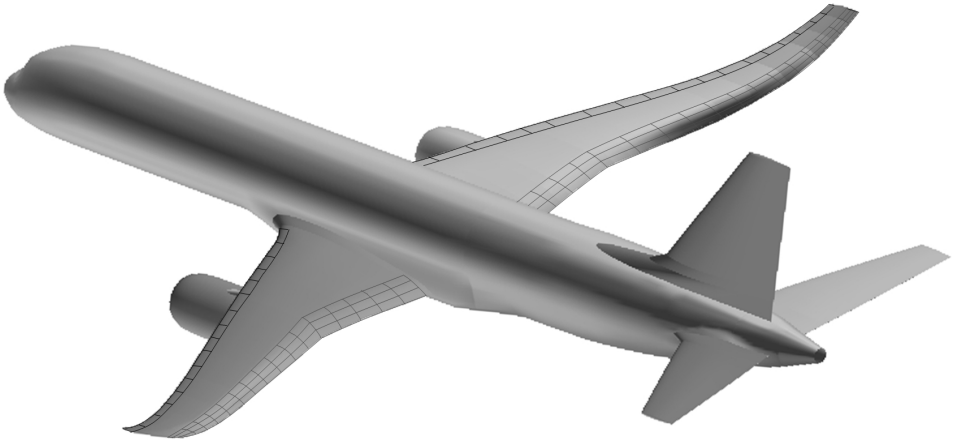

Fig. 1 - Variable Camber Continuous Trailing Edge Flap (VCCTEF) System on Flexible Wing Aircraft

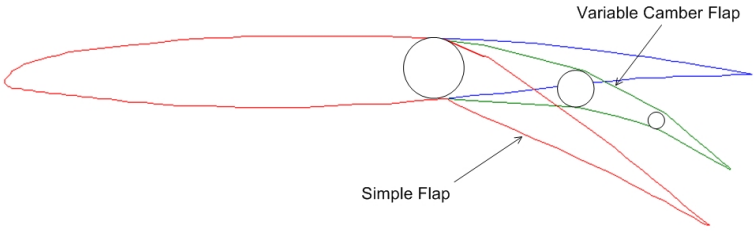

Fig. 2 - Three Chordwise-Segment Variable Camber Flap

The flap chord of the VCCTEF is comprised of three chordwise segments of equal chord length, as shown in Fig. 2. These three chordwise flap segments can be individually commanded or actuated in unison when a flap deflection command is given. By varying the deflections of the individual chordwise flap segments, any camber surface can be created to achieve a desired aerodynamic performance. In general, a cambered flap is more efficient in producing lift than a straight conventional flap by achieving lift at lower drag. The continuous trailing edge flap is comprised of multiple spanwise flap sections, as shown in Fig. 1, to form a continuous trailing edge when the flap is deflected. The continuous trailing edge flap is used to optimize the spanwise lift distribution to improve aerodynamic efficiency. Furthermore, this continuous trailing edge would eliminate vortices which otherwise would have formed at the conventional flap discontinuity in the trailing edge region. By eliminating vortex formation, viscous drag losses as

well as acoustic noise from turbulence could be attenuated. Thus, this feature further provides a drag reduction benefit in addition to the variable camber feature. An aircraft wing equipped with the VCCTEF can be shaped adaptively to attain optimal aerodynamic performance throughout a flight envelope.

Following the initial NASA Innovation Fund study, Boeing Research & Technology conducted a joint study with NASA to develop a revised VCCTEF design[3,4] as shown in Fig. 3. This study was built upon the development of the original VCCTEF system for NASA Generic Transport Model (GTM) which is essentially based on the Boeing 757 airframe, employing light-weight shaped memory alloy (SMA) technology for actuation and three separate chordwise segments shaped to provide a variable camber to the flap. This cambered flap has potential for drag reduction as compared to a conventional straight, plain flap. The flap is also made up of individual 2-foot spanwise sections which enable different flap setting at each flap spanwise position. This results in the ability to control the wing twist shape as a function of span, resulting in a change to the wing twist to establish the best lift-to-drag ratio (L/D) at any aircraft gross weight or mission segment. Wing twist on traditional commercial transport designs is dictated by the aeroelastic deflection of a fixed "jig twist" shape applied at manufacture. The design of this jig twist is set for one cruise configuration, usually for a 50% fuel loading or mid-point on the gross weight schedule. The VCCTEF offers different wing twist settings, hence different spanwise loadings, for each gross weight condition and also different settings for climb, cruise and descent, a major factor in obtaining best L/D conditions.

The second feature of VCCTEF is a continuous trailing edge flap. The individual 2-foot spanwise flap sections are connected with a flexible covering, so no breaks can occur in the flap planforms, thus reducing drag by eliminating these breaks in the flap continuity which otherwise would generate vorticity that results in a drag increase and also contributes to airframe noise. This continuous trailing edge flap design combined with the flap camber result in lower drag increase during flap deflections. In addition, it also offers a potential noise reduction benefit.

The revised VCCTEF design includes 14 sections attached to the outer wing and 3 sections attached to the inner wing, as shown in Fig. 3.[4] Each 24-inch section has three chordwise cambered flap segments that can be individually commanded. These cambered flaps are joined to the next section by a flexible and supported material (shown in blue) installed with the same shape as the camber and thus providing continuous flaps throughout the wing span with no drag producing gaps.

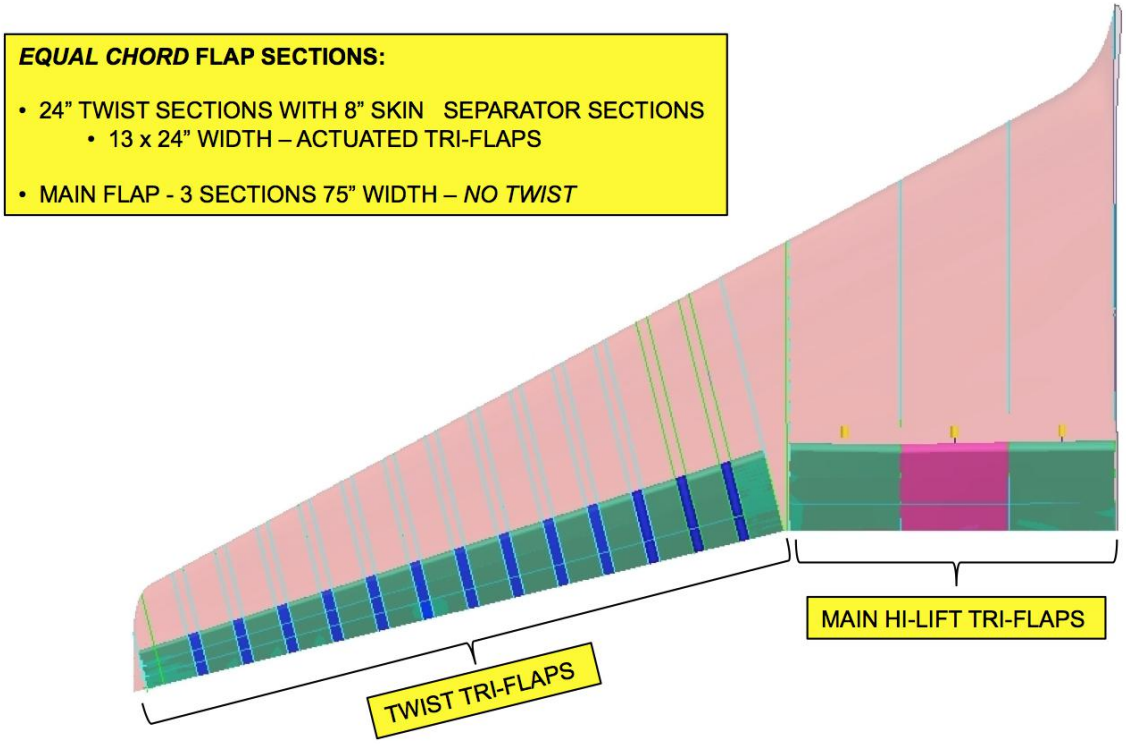

Fig. 3 - GTM Wing Configured with the Variable Camber Continuous Trailing Edge Flap

Using the camber positioning, a full-span, low-drag, high-lift configuration can be activated that has no drag producing gaps and a low flap noise signature. This is shown in Fig. 4. To further augment lift, a slotted flap

configuration is formed by an air passage between the wing and the inner flap that serves to improve airflow over the flap and keep the flow attached. This air passage appears only when the flaps are extended in the high lift configuration.

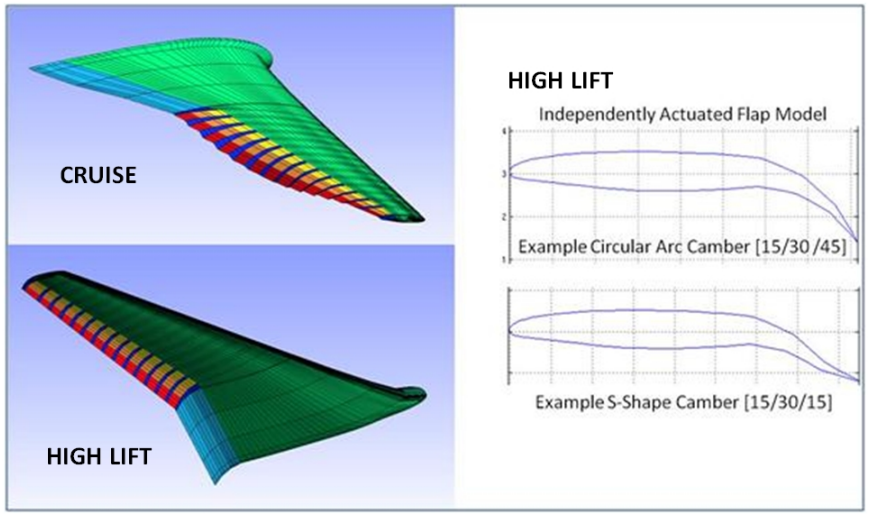

Fig. 4 - Cruise and High Lift VCCTEF Configurations

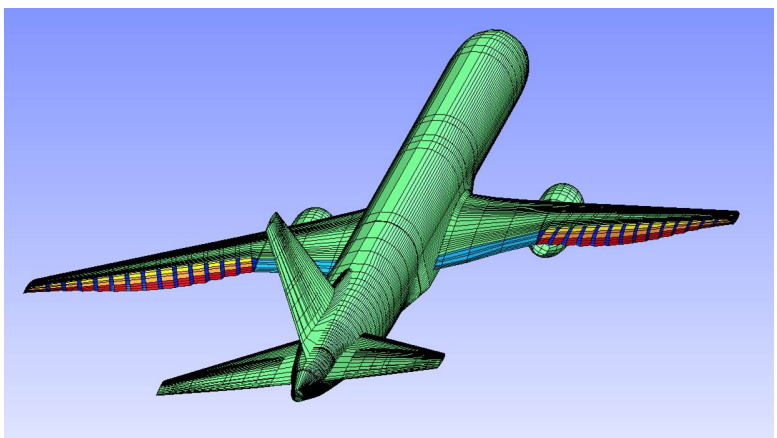

Fig. 5 - GTM with VCCTEF

Figure 5 illustrates the GTM equipped with the VCCTEF for wing shaping control. By actively shaping the wing aerodynamic surface using the VCCTEF, optimal aerodynamic performance could potentially be realized at any point in the flight envelope. The VCCTEF relies on two mechanisms to improve aerodynamic performance: 1) wing twist optimization for flexible wing design, and 2) variable camber and continuous trailing edge for improved aerodynamics. This fixed-wing technology may be referred to as Performance Adaptive Aeroelastic Wing (PAAW) technology.

The performance of an adaptive wing can be described by the following equation:[5]

$$\alpha_c(y) = \alpha\left[1 - \frac{\partial\Theta(\bar{y})}{\partial\alpha}\cos\Lambda - \frac{\partial}{\partial\alpha}\left(\frac{dW(\bar{y})}{d\bar{y}}\right)\sin\Lambda\right] - \alpha_i(y) - \gamma(\bar{y})\cos\Lambda - \Theta_0(\bar{y})\cos\Lambda - \frac{dW_0(\bar{y})}{d\bar{y}}\sin\Lambda$$
$$+\sum_{i=1}^{N}\left[\frac{\partial\alpha_c}{\partial\delta_i}\cos\Lambda_h - \frac{\partial\Theta(\bar{y})}{\partial\delta_i}\cos\Lambda - \frac{\partial}{\partial\delta_i}\left(\frac{dW(\bar{y})}{d\bar{y}}\right)\sin\Lambda\right]\delta(y_h) \tag{1}$$

where α_c is the sectional angle of attack, α is the geometric angle of attack of the wing section about the pitch axis y, α_i is the induced angle of attack due to the downwash about the pitch axis y, γ is the wing pre-twist angle about the elastic axis $\bar{y} = y/\cos\Lambda$ (positive nose down), Θ is the wing torsional twist about the elastic axis $\bar{y}$ (positive nose down), W is wing vertical bending along the elastic axis (positive upward), Λ is the sweep angle of the elastic axis, δ_i is the absolute deflection of the i-th flap segment of the VCCTEF about the hinge axis y_h which has a sweep angle of Λ_h, and $\partial\alpha_c/\partial\delta_i$ is the angle of attack sensitivity or camber control derivative due to the VCCTEF flap deflection.

It can be seen that the aeroelastic deflections can cause the desired sectional angle of attack to be non-optimal. The effect of the adaptive aeroelastic wing shaping control by the VCCTEF is captured in the last term. The term $\partial\alpha_c/\partial\delta_i$ is the rigid camber control to compensate for the non-optimal sectional angle of attack. The two terms $\partial\Theta/\partial\delta_i$ and $\partial\left(dW/d\bar{y}\right)/\partial\delta_i$ are the aeroelastic wing shaping control by leveraging wing flexibility to change the wash-out twist of a wing in order to achieve improved aerodynamic performance. Thus, the effect of adaptive aeroelastic wing shaping control is to optimize the span load at any operating point inside a given flight envelope.

The flexibility of modern transport wings can cause a reduction in flutter margins which can compromise aircraft stability. Equivalently, a flexible wing is more responsive to gust or maneuver loads which can lead to structural issues as well as compromised ride and handling qualities. In a previous study, a flutter analysis was conducted to examine the effect of increased flexibility of the GTM wing.[6] The baseline wing stiffness of the GTM is reduced by 50%. This reduced-stiffness GTM wing is referred to as the Elastic Shaped Aircraft Concept (ESAC) wing for differentiation. Table 1 shows the flutter speed prediction at 35,000 ft for the GTM wing and the ESAC wing. The critical flutter modes for the GTM wing and ESAC wing are the first anti-symmetric bending mode. The flutter speed prediction is also compared against NASTRAN doublet lattice solution which gives a flutter speed of Mach 0.954 for the ESAC wing at 35,000 ft corresponding to the first anti-symmetric bending mode at a frequency of 2.53 Hz. This represents a 3% difference which demonstrates an excellent agreement.

	Symmetric Mode	Anti-Symmetric Mode
GTM Flutter Mach @ 35K ft	1.358	1.310
GTM Flutter Frequency @ 35K ft, Hz	4.31	3.87
ESAC Flutter Mach @ 35K ft	0.938	0.925
ESAC Flutter Frequency @ 35K ft, Hz	6.94	2.85

Table 1 - Flutter Speed Prediction

The FAA certification requires a flutter margin of at least 15% above the dive speed which is normally determined from flight testing. In this study, the dive speed may be estimated to be about 20% over the maximum operating Mach of 0.8, which yields a dive speed of Mach 0.96. Thus, the flutter clearance requires a flutter speed of at least Mach 1.10 at 35,000 ft. The GTM wing demonstrates to meet this flutter clearance but not the ESAC wing. Thus, active flutter suppression control may be required as wing flexibility increases. In practice, active flutter suppression could be difficult to certify since aircraft must demonstrate to be open-loop stable. Also, active flutter suppression control will require power which could offset any potential aerodynamic performance benefits from wing shaping control using the VCCTEF. Nonetheless, currently there appears to be an interest in certification of active flutter suppression for flight control systems.

To address the adaptive aeroelastic wing shaping control objective, a multidisciplinary design analysis optimization (MDAO) framework must be considered by incorporating the aerodynamic performance prediction together with aeroelasticity and flutter suppression control. The objective of the MDAO is to identify a desired wing flexibility that would provide the best overall aerodynamic, aeroelasticity, and control benefits. For example, the wing stiffness could be reduced to an optimal value that would maximize the aerodynamic performance at off-design cruise with the least amount of control effort to maintain aeroelastic stability margin. The MDAO would also include control gain synthesis directly in the MDAO process.

To explore the effect of stiffness reduction on the flutter speed, a sensitivity study is conducted to determine the flutter boundary as a function of the ESAC wing torsional stiffness GJ while the ESAC wing bending stiffness EI is kept at half of that of the GTM wing. Figure 6 shows the flutter boundary for a varying torsional stiffness from 100% to 50% of that of the GTM wing. It can be seen from Fig. 7 that to clear the flutter boundary at Mach 1.1, the ESAC wing torsional stiffness GJ cannot be reduced to less than 65% of that of the GTM wing. The question to be investigated is whether or not there are any additional aerodynamic performance benefits by reducing the torsional stiffness GJ further in exchange for the need to incorporate active flutter suppression control. Another question to be investigated is how much power is consumed by active flutter suppression control that could offset potential drag reduction benefits. These questions are aircraft design consideration that need to be investigated holistically in order to realize a synergistic integrated solution that combines flight control consideration into the aerodynamics and aeroelasticity disciplines.

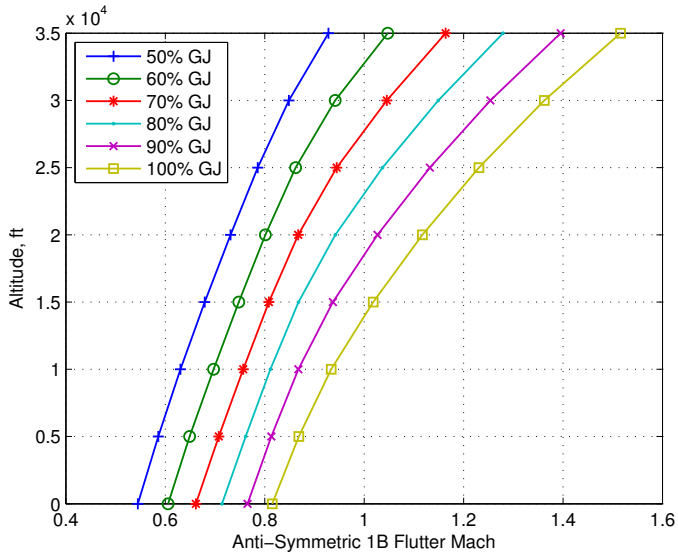

Fig. 6 - Flutter Boundary of ESAC Wing as a Function of *GJ*

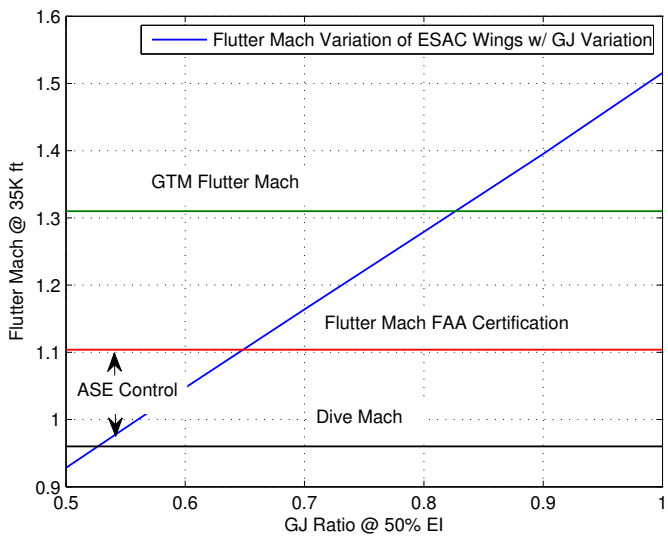

Fig. 7 - Flutter Mach Clearance of ESAC Wing

Flight control design of conventional aircraft has a long heritage with pitch control by an elevator, roll control by an aileron, and yaw control by a rudder. As new control effectors become available for PAAW technology, a new flight control paradigm should be considered. In the presence of multiple control surfaces such as the VCCTEF, the single-objective flight control tasks such as a pitch command need to be re-examined. In the presence of increased wing flexibility, the conventional rigid-body pitch control design may become insufficient since any aircraft maneuvers can potentially excite aeroelastic modes. Currently, in a conventional flight control design, this is addressed passively via aeroservoelastic (ASE) notch filtering. Maneuver loads can potentially limit how fast a maneuver can be commanded. Given the availability of multiple control surfaces, a typical pitch control design would have to consider additional requirements: 1) minimum drag during pitch, 2) aeroelastic mode suppression, 3) maintaining wing root bending and pitching moments from aeroelastic responses to within the allowable limits, 4) maintaining acceptable pilot handling qualities based on frequency and damping of the aircraft rigid-body longitudinal modes, and perhaps other requirements.

To address all of these flight control objectives simultaneously can be a challenging flight control design. A multi-objective optimization framework can be developed to address the needs for satisfying multiple, competing

flight control requirements. This paper will present a multi-objective flight control approach to address some of these multi-disciplinary interactions in a flexible wing aircraft employing PAAW technology. A multi-objective flight control system is proposed to simultaneously gain aerodynamic efficiency and maintain traditional pilot command-tracking tasks for guidance and navigation. A multi-objective optimal control design will be developed to address drag minimization during maneuvers in conjunction with aeroelastic mode suppression control.

II. Adaptive Aeroelastic Wing Shaping Control

The elastically shaped aircraft concept is modeled as a notional single-aisle, mid-size, 200-passenger aircraft. The geometry of the ESAC is obtained by scaling up the geometry of NASA Generic Transport Model (GTM) to full scale. The reason for selecting the GTM is that there already exists an extensive wind tunnel aerodynamic database that could be used for validation in the study. The benchmark configuration represents one of the most common types of transport aircraft in the commercial aviation sector that provides short-to-medium range passenger carrying capacities.

The aircraft has a take-off weight of 200,000 lbs for a typical operating load (gear up, flap up) that includes cargo, fuel, and passengers. Fuel weighs about 50,000 lbs for a range of about 3,000 nautical miles. The aircraft is powered by two 44,000-lb rated turbofan engines. The maximum thrust per engine at sea level take-off is 44,000 lbs and varies linearly to 30,000 lbs at sea level Mach 0.8 The thrust specific fuel consumption (TSFC) at sea level take-off is 0.3460 /hr and varies linearly to 0.6656 /hr at sea level Mach 0.8. The total maximum engine thrust and TSFC as functions of altitude and Mach number can be estimated by the following formulas:

$$T_{max}(h,M) = (-77031M + 100986)\left(1 + \frac{\gamma - 1}{2}M^2\right)^{\frac{\gamma}{\gamma-1}} \delta(h) \tag{2}$$

$$c(M,h) = (0.45642M + 0.26156)\sqrt{\theta(h)\left(1 + \frac{\gamma - 1}{2}M^2\right)} \tag{3}$$

where T_{max} is the maximum thrust, c is the TSFC, M is Mach number, $\delta = p/p_{SL}$ is the pressure ratio, $\theta = T/T_{SL}$ is the temperature ratio, and p_{SL} and T_{SL} are the pressure and temperature at sea level.

Aeroelastic deflection can affect aircraft aerodynamics. As an aircraft cruises, fuel is burned and the wing loading is reduced, thereby causing the wing shape to change. The change in wing shape can cause a drag penalty since the wing shape no longer retains its optimal design shape. This particularly can be an important issue for light-weight airframes. Thus, aircraft with flexible wing structures can potentially become less fuel-efficient if there is no mechanism to compensate for aeroelastic deflection. Fig. 8 illustrates notional drag polars estimated by an aerodynamic model at three points in the cruise envelope corresponding to 80%, 50%, and 20% fuel loading.[1] The midpoint of cruise that corresponds to 50% fuel loading is considered to be the wing optimal design point. The initial analysis indicate a significant drag penalty as the wing shape moves away from its optimal shape.

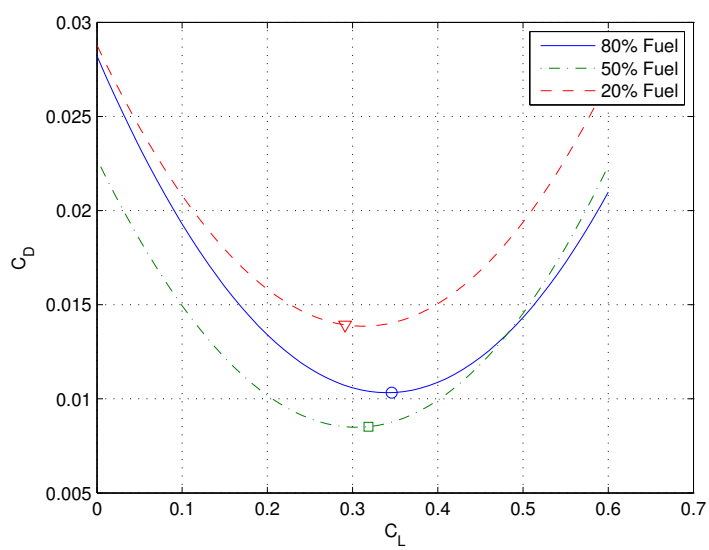

Fig. 8 - Drag Penalty due to Aeroelastic Deflection

Since aeroelasticity can adversely affect the trim drag coefficient at cruise, in order to maintain the best cruise efficiency, the wing shape would need to be actively controlled. This problem is well recognized in modern transport aircraft design such as the Boeing 787 which is equipped with active wing twist control. As the wing operates at off-design cruise flight conditions, the VCCTEF is deployed to optimize span load to achieve minimum induced drag. This problem can be solved by a coupled aerodynamic-aeroelastic optimization. Initial optimization studies have identified a potential significant drag reduction of the VCCTEF.[7] Furthermore, a low-speed wind tunnel experiment was conducted at University of Washington Aeronautical Laboratory (UWAL) in 2013 to test a 10% scaled model of the flexible GTM wing configured with the VCCTEF.[5] The wind tunnel test also identified drag reduction benefits of the VCCTEF.[5]

Off-line optimization can be used to establish a schedule of flap settings based on aircraft weight and flight conditions. However, during cruise, variances in aircraft gross weight and operating conditions can result in different performance characteristics than the optimal solutions provided by off-line optimization. Thus, an integrated strategy in multi-objective flight control is to incorporate a real-time drag optimization to compensate for operating variances. This real-time drag optimization could leverage wing shape measurements for estimating the operating local angles of attack. This information is then used to determine the VCCTEF settings to compensate for the operating variances in real time.

III. Multi-Objective Flight Control for Drag Reduction

Multi-objective flight control design is an enabling feature of PAAW technology. A typical flight control design usually takes into account different sets of requirements for performance and stability that must be considered during a design process. Performance in the context of flight control usually implies the ability for a flight control system to follow a pilot command. However, in this study, a new notion of aerodynamic performance is introduced into the flight control framework. The goal of the new vehicle is to achieve low drag through adaptive aeroelastic wing shaping control actuation. Thus, drag penalty due to the VCCTEF should be considered in a flight control design. Hence, a new concept of multi-objective flight control is proposed to not only achieve a pilot command-following objective but also a drag reduction objective[1] during maneuvers such as a pitch command or roll command.

Stability is of paramount importance for any flight vehicle. Structural flexibility of airframes including wings can cause significant aeroelastic interactions that can degrade vehicle stability margins, potentially leading to loss of control. There exists a trade-off between the desire of having light-weight, flexible structures for weight savings and the need for maintaining sufficient robust stability margins from aeroelastic stability perspectives. For flexible wing aircraft, the flutter speed boundary can occur below FAA flutter clearance. Thus, a flight control system must be able to stabilize aeroelastic modes. The VCCTEF system must be designed to achieve this objective. For obvious reasons, it is not acceptable to operate an unstable transport vehicle that relies on feedback control for closed-loop stability. Thus, in practice, passive aeroelastic tailoring in the design process can be used to increase flutter margins. Then, the role of a flight control system would be relegated to stability augmentation as opposed to a more demanding task of stabilization. This is considered more acceptable in the certification framework as aircraft flight control systems already have many stability augmentation design features built in such as yaw and pitch dampers to provide desired damping characteristics to meet pilot handling quality requirements.

Gust and maneuver load alleviation control is also an important part of the overall flight control strategy for flexible aircraft. As flexibility increases, the vehicle aeroelastic response to wind gust disturbances or during a maneuver can result in handling and ride quality issues. Gust load alleviation control will reduce the aeroelastic response by reactive feedback control or predictive feedforward control using early detection turbulence sensors. Similarly, maneuver loads can be kept to within the load envelope by means of maneuver load alleviation control.

In terms of control actuation, the VCCTEF is designed with dual purposes. The two inner chordwise flap segments are driven by shaped memory alloy (SMA) actuators which are slow actuators suitable only for changing the VCCTEF settings for cruise drag optimization either by scheduling or real-time drag optimization. This is considered a guidance feature. For fast-acting flight control functions, the outermost chordwise flap segment is designed to be a fast acting control surface driven by electro-mechanical actuators (EMA). This flap segment is spanned the entire wing and is assumed to have sufficient bandwidth and control power for roll control and aeroelastic mode suppression control.

The multi-objective flight control framework is envisioned to comprise of the following objectives all acting in a synergistic manner: 1) traditional pilot command-following flight control, 2) drag minimization, 3) aeroelastic mode suppression, and 4) gust and maneuver load alleviation. Each of these objectives can be a major control system design in its own rights. Thus, a multi-objective flight control system can be a complex flight control design that takes into

account multiple competing requirements to achieve optimal flight control solutions that have the best compromise for these requirements. Figure 9 illustrates an architecture of a multi-objective flight control system.

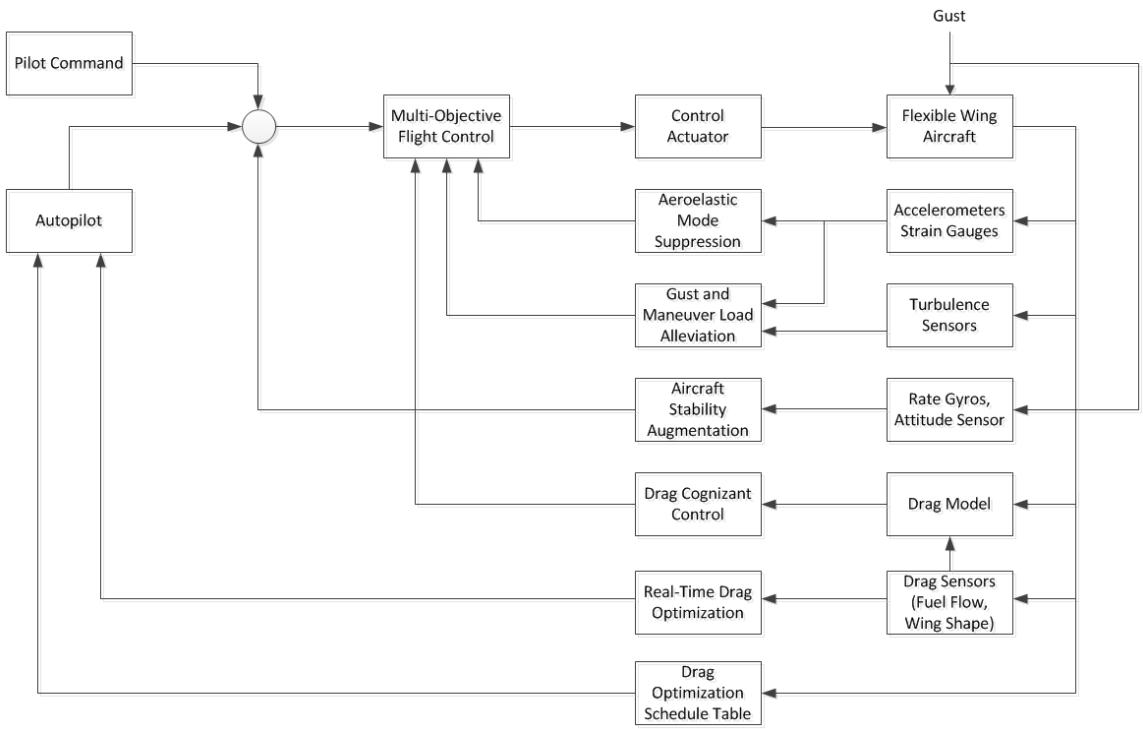

Fig. 9 - Multi-Objective Flight Control Architecture

In this study, we will consider the first three objectives. We will simplify some aspects of flight control design with a purpose of better illustrating the key salient concepts as opposed to illuminating the detail control theory. Traditional aircraft flight control is well understood, so the focus will be on aeroelastic mode suppression and drag minimization control.

A. Coupled Flight Dynamic and Aeroservoelastic state-space Model

A coupled flight dynamic and aeroservoelastic (ASE) model of the ESAC was developed. It consists of a nonlinear six-degree-of-freedom (6-DOF) flight dynamic model, a linear aeroelastic model of the flexible wing, and a linear actuator model of the VCCTEF. Unsteady aerodynamics of the flexible wing and the high-bandwidth control surfaces are accounted for by means of aerodynamic lag states.[8,9] These lag states are used to approximate Theodorsen's function, so that a frequency-independent state-space realization can be formulated. The lag state dynamics are determined by the frequency-domain rational fraction approximation of Theodorsen's function

$$C(k) \approx \bar{C}(k) = \frac{b_n (ik)^n + b_{n-1} (ik)^{n-1} + \cdots + b_1 (ik) + b_0}{(ik)^n + a_{n-1} (ik)^{n-1} + \cdots + a_1 (ik) + a_0} \tag{4}$$

where n is the order of the approximation.

Increasing the order of the approximation increases accuracy, but also increases the required number of lag states. For each order of the approximation, two lag states are added for each elastic mode and two are added for each control surface. Consequently, the number of states will rapidly grow as the order of the approximation increases. For the purpose of control design, the full-order model is linearized about a trimmed cruise condition, resulting in a linear coupled flight dynamic and ASE state-space model of the form

$$\begin{bmatrix} \dot{x}_r \\ \dot{x}_e \\ \dot{x}_f \end{bmatrix} = \begin{bmatrix} A_r & A_{re} & A_{rf} \\ A_{er} & A_e & A_{ef} \\ A_{fr} & A_{fe} & A_f \end{bmatrix} \begin{bmatrix} x_r \\ x_e \\ x_f \end{bmatrix} + \begin{bmatrix} B_r & 0 \\ 0 & 0 \\ 0 & B_f \end{bmatrix} \begin{bmatrix} u_r \\ u_f \end{bmatrix} \tag{5}$$

$$y = \begin{bmatrix} C_r & C_e & C_f \end{bmatrix} \begin{bmatrix} x_r \\ x_e \\ x_f \end{bmatrix} + \begin{bmatrix} D_r & D_f \end{bmatrix} \begin{bmatrix} u_r \\ u_f \end{bmatrix} \tag{6}$$

where x_r is the aircraft rigid-body state vector, x_e is the elastic state vector, x_f is the VCCTEF state vector, $u_r = \begin{bmatrix} \delta_e & \delta_r & \delta_T \end{bmatrix}^\top$ are the aircraft rigid-body flight control command vector comprising the elevator δ_e, the rudder δ_r, and the engine thrust δ_T, u_f is the deflection command vector for VCCTEF control surfaces, and y is the output vector which is defined by the sensor system and will be addressed in that context.

The rigid-body state x_r contains the usual states of a 6-DOF flight dynamic model, and the engine thrust, elevator, and rudder states. The elastic state vector $x_e = \begin{bmatrix} \eta & \dot{\eta} & y_\eta & z_\eta \end{bmatrix}^\top$ contains two generalized states η and $\dot{\eta}$, as well as the aerodynamic lag states for each mode. The aerodynamic lag states are also expressed in the generalized coordinates. The lag states corresponding to η are indicated by y_η, and those corresponding to $\dot{\eta}$ are indicated by z_η.

The outermost flap segments of the VCCTEF are high-bandwidth control surfaces that are joined to the elastic wing via the two inner chordwise flap segments which are assumed to be rigid during a flight control actuation. For slow dynamics associated with rigid-body aircraft flight dynamics, the control surface deflection δ is sufficient for flight control. However, for flexible wing dynamics, the dynamics of a control surface described by its rate $\dot{\delta}$ and its acceleration $\ddot{\delta}$ can be very significant and therefore cannot be neglected. Consequently, a model based on the assumptions of quasi-steady aerodynamics and an ideal actuator is unable to sufficiently capture the control surface high-frequency dynamics and their interactions with the elastic wing. In order to address this, the VCCTEF model incorporates servo and control surface dynamics, and the corresponding aerodynamic lag states.

An overview of the VCCTEF model is given in Fig. 10. The VCCTEF state vector $x_f = \begin{bmatrix} \delta & \dot{\delta} & y_\delta & z_\delta & T & x_I \end{bmatrix}^\top$ contains all state variables concerned with the VCCTEF model, namely the deflection states δ and $\dot{\delta}$ and their respective aerodynamic lag states y_δ and z_δ, the motor torque T for each flap, and the PID integrator state x_I for the VCCTEF actuator control system.

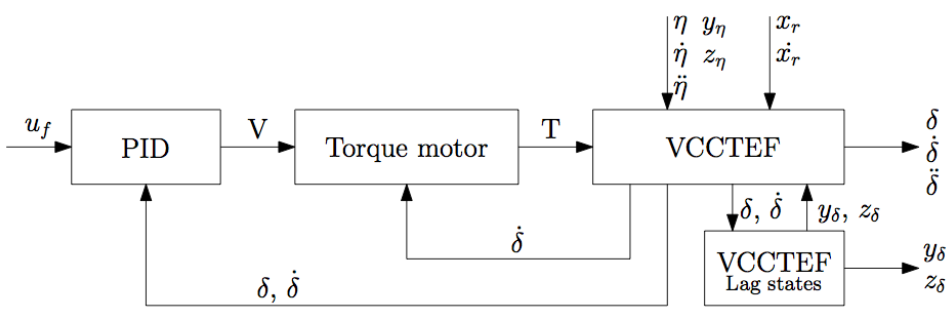

Fig. 10 - Overview of VCCTEF Model

The VCCTEF dynamics are described by a second-order differential equation that is coupled to the rigid-body and aeroelastic wing states as follows:

$$I\ddot{\delta} + C\dot{\delta} + K\delta = M_{x_r}x_r + M_{x_{\dot{r}}}x_{\dot{r}} + M_\eta \eta + M_{\dot{\eta}}\dot{\eta} + M_{\ddot{\eta}}\ddot{\eta} + M_{y_\eta}y_\eta + M_{z_\eta}z_\eta + M_{y_\delta}y_\delta + M_{z_\delta}z_\delta + T \tag{7}$$

The matrices I, C, and K are the structural and aerodynamic inertia, damping and stiffness matrices of the system, respectively. The aerodynamic hinge moment is also due to the rigid-body state and its derivative, the elastic state, its derivatives and aerodynamic lag states, and the VCCTEF aerodynamic lag states. In Fig. 10, it can be seen that the VCCTEF model output not only consists of the deflection δ, but also of the deflection rate $\dot{\delta}$ and acceleration $\ddot{\delta}$, and the lag states y_δ and z_δ. All of these outputs are used to calculate the unsteady aerodynamic contributions of the VCCTEF to the rigid-body and elastic state equations.

B. Model Reduction

The full-order coupled flight dynamic and ASE model includes a high number of elastic modes along with corresponding aerodynamic lag states, as well as dynamic, servo and aerodynamic lag states for the 32 VCCTEF elements.

Consequently, the full model has a very large number of states. If a second-order approximation for unsteady aerodynamics is applied, the total number of states in the ASE state-space model is equal to 1461.

In general, an ASE state-space model contains both rigid-body modes which usually have low frequencies, and aeroelastic modes which are at much higher frequencies than the rigid-body modes. Flutter modes are usually associated with those aeroelastic modes in the low frequency range. As a result, high frequency aeroelastic modes normally do not participate in a flutter response. In control design, it is usually expedient to remove high frequency modes in order to simplify a controller design. By removing the high frequency aeroelastic modes, the ASE state-space model is reduced in order. Balanced realization is a popular technique for model reduction. In this paper, we will employ a singular perturbation method to reduce the order of an ASE state-space model.[10]

Consider the state-space model given in Eqs. (5) and (6), now rearranged in the form

$$\begin{bmatrix} \dot{\xi} \\ \dot{\mu} \end{bmatrix} = \begin{bmatrix} A_{11} & A_{12} \\ A_{21} & A_{22} \end{bmatrix} \begin{bmatrix} \xi \\ \mu \end{bmatrix} + \begin{bmatrix} B_1 \\ B_2 \end{bmatrix} u \tag{8}$$

$$y = C_1\xi + C_2\mu + Du \tag{9}$$

where μ is a fast state vector, ξ is a slow state vector, and $u = \begin{bmatrix} u_r & u_f \end{bmatrix}^\top$.

The quality of fast and slow states can be examined by the eigenvalues of the partitioned matrices A_{11} and A_{22}. Since $\mu(t)$ is a fast state vector, we can write $\|A_{11}\| < \varepsilon \|A_{22}\|$. Using the singular perturbation approach, the fast and slow dynamics can be decoupled. To decouple the fast and slow states, we perform a time-scale separation by applying the singular perturbation method. Toward that end, we consider a slow time transformation

$$\tau = \varepsilon t \tag{10}$$

where τ is a slow time variable.

Then, the fast and slow state-space models are transformed into a singularly perturbed system as

$$\dot{\xi} = A_{11}\xi + A_{12}\mu + B_1 u \tag{11}$$

$$\varepsilon \frac{d\mu}{d\tau} = A_{21}\xi + A_{22}\mu + B_2 u \tag{12}$$

The Tikhonov's theorem can be used to approximate the solution of the singularly perturbed system with the solution of a "reduced-order" system by setting $\varepsilon = 0$.[11] Thus, the reduced-order system is given by

$$\dot{\xi}_0 = A_{11}\xi_0 + A_{12}\mu_0 + B_1 u \tag{13}$$

$$A_{21}\xi_0 + A_{22}\mu_0 + B_2 u = 0 \tag{14}$$

where ξ_0 and μ_0 are the "outer" solution of the singularly perturbed system.

The term "outer" is in connection with the concept of "inner" or "boundary layer" and "outer" solutions which have the origin in boundary layer theory due to Prandtl. The "inner" or "boundary layer" solution for this system is obtained from

$$A_{11}\xi_i + A_{12}\mu_i + B_1 u = 0 \tag{15}$$

$$\dot{\mu}_i = A_{21}\xi_i + A_{22}\mu_i + B_2 u \tag{16}$$

The solution is then expressed as

$$\xi = \xi_0 + \xi_i - \xi_{MAE} \tag{17}$$

$$\mu = \mu_0 + \mu_i - \mu_{MAE} \tag{18}$$

where $\xi_{MAE}(t)$ and $\mu_{MAE}(t)$ are correction terms by a matched asymptotic expansion method applied to both the inner and outer solutions.[12] The outer solution is in fact the asymptotic solution of the original system as $t \to \infty$.

Since the asymptotic behavior of a closed-loop system is an important consideration for stability implication, the outer solution of the singularly perturbed system is of significant importance. Thus, we obtain the outer solution as the reduced-order model using only the outer solution of the slow state vector ξ_0 as

$$\dot{\xi}_0 = \underbrace{\left(A_{11} - A_{12}A_{22}^{-1}A_{21}\right)}_{\bar{A}} \xi_0 + \underbrace{B_1 - A_{12}A_{22}^{-1}B_2}_{\bar{B}} u + \Delta\dot{\xi}_0 \tag{19}$$

$$y = \underbrace{\left(C_1 - C_2A_{22}^{-1}A_{21}\right)}_{\bar{C}_1} \xi_0 + \underbrace{\left(D_1 - C_2A_{22}^{-1}B_2\right)}_{\bar{D}_1} u + \Delta y \tag{20}$$

C. VCCTEF Virtual Control Variables

All the control surfaces are not entirely independent in their motions due to the physical constraints imposed by the elastomer transition material. This material has certain position and rate limits. Thus, the control surfaces will have relative position and rate limits. These limits are not the normal position and rate limits that actuators are subjected to. Thus, these relative constraints can cause challenges in a control design of this system.

Consider the following relative constraints

$$|\delta_{i+1} - \delta_i| \leq \Delta\delta \tag{21}$$

$$\left|\dot{\delta}_{i+1} - \dot{\delta}_i\right| \leq \Delta\dot{\delta} \tag{22}$$

where $i = 1, 2, \ldots, M$ is the index of each flap section, and M is the number of spanwise sections of the VCCTEF per wing.

For the VCCTEF design, the relative motion between any pair of adjacent flap sections is allowed to be within 2 degrees. The rate constraint imposed by the elastomer material is not yet defined and thus is assumed to be large.

To address the relative position limit, a concept of virtual control has recently been introduced.[13] The control surface deflections are described by a shape function. This shape function can be any reasonable shape function with a smooth and gradual slope. Suppose the ideal continuous trailing edge of the VCCTEF is mathematically smooth and can be described by a Fourier sine series as follows:

$$\delta^*(x) = A_0 + \sum_{n=1}^{N} A_n \sin\frac{n\pi x}{L} \tag{23}$$

where $\delta^*(x)$ is a theoretical VCCTEF deflection and N is the number of terms in the Fourier sine series

In practice, the trailing edge of the VCCTEF is only stepwise continuous due to the physical implementation. Therefore, the actual VCCTEF deflection is a stepwise linear approximation of the theoretical VCCTEF deflection. Thus

$$\delta_i = A_0 + \sum_{n=1}^{N} A_n \sin\frac{(i-1)n\pi}{N-1} \tag{24}$$

where i is the flap index.

Note that A_0 is the constant flap deflection which is needed to provide flexibility for multi-objective flight control, especially for drag reduction control. The constant flap deflection at the wing tip can be used to create a zero lift condition to minimize tip vortices. The quantities A_n, $n = 0, 1, \ldots, N$ can be viewed as virtual control variables. The virtual control variables are then used in a flight control design to determine their command settings. Then, the actual VCCTEF deflection command u_f can be computed from the virtual control commands A_n. Since Eq. (24) is linear in the virtual commands, a transformation matrix that relates u_f to u_v can be constructed straightforwardly using the partial derivatives with respect to the virtual commands. Note that the constraint is independent for both wings, so the vector of VCCTEF virtual control variables for both wings, u_v , has $2 \times N$ elements.

D. Multi-Objective Optimal Control

Consider a flight control design for a flight path angle command. Let $x_a = \int_0^t \Delta\gamma d\tau$ be an integral error state of the flight path angle, where the error between the flight path angle and its command signal is expressed as

$$\Delta\gamma = \theta - \alpha - \gamma_c = A_a x_r - \gamma_c \tag{25}$$

where γ_c is a commanded flight path angle.

Let $x = \begin{bmatrix} x_r & x_r & x_f & x_a \end{bmatrix}^\top$ where $\begin{bmatrix} x_r & x_r & x_f \end{bmatrix}^\top$ is the partitioned state of the reduced-order model, and $u = \begin{bmatrix} u_r & u_v \end{bmatrix}^\top$, then the augmented plant is expressed as

$$\dot{x} = Ax + Bu + z \tag{26}$$

where

$$A = \begin{bmatrix} A_r & A_{re} & A_{rf} & 0 \\ A_{er} & A_e & A_{ef} & 0 \\ A_{fr} & A_{fe} & A_f & 0 \\ A_a & 0 & 0 & 0 \end{bmatrix}, \; B = \begin{bmatrix} B_r & 0 \\ 0 & 0 \\ 0 & B_v \\ 0 & 0 \end{bmatrix}, \; z = \begin{bmatrix} 0 \\ 0 \\ 0 \\ -\alpha_c \end{bmatrix} \tag{27}$$

is based on the reduced-order model.

An optimal control is designed with the following multi-objective cost function[13]

$$J = \frac{1}{2}\int_0^{t_f} \left(x_r^\top Q_r x_r + x_e^\top Q_e x_e + x_f^\top Q_f x_f + x_a^\top Q_a x_a + u^\top R u + q_D \Delta C_D \right) dt \tag{28}$$

where $Q_r > 0$, $Q_e > 0$, $Q_f > 0$, $Q_a > 0$, $R > 0$, and $q_D > 0$.

The first term in the cost function is designed to bound the rigid-body states, the second term to damp out aeroelastic modes, the third term to minimize the flap states, the fourth term to track the command signal α_c, and the fifth term to minimize the control effort. Hence, the first five terms in the cost function form the standard linear-quadratic regulator (LQR) cost function. The last term is designed to minimize the drag coefficient with q_D as a weighting constant. The coefficient ΔC_D represents the increase in drag relative to the drag in trim condition.

It is assumed that the drag coefficient can be estimated accurately via a drag polar model for which the drag polar parameters are known. The model is derived using aerodynamic strip theory. The wing, fuselage, and horizontal tail surface are divided into strips for which the local drag derivatives are calculated. The total drag polar model can be expressed as

$$C_D = C_{D_0} + \left(C_{L_0} + C_{L_x} x + C_{L_{\dot{x}}} \dot{x}\right)^\top K \left(C_{L_0} + C_{L_x} x + C_{L_{\dot{x}}} \dot{x}\right) \tag{29}$$

where K is a diagonal matrix containing the drag polar parameter of each strip, C_{D_0} is a scalar value representing the zero-lift drag coefficient, C_{L_0} is a column vector containing the trim state lift coefficient of each strip, and C_{L_x} and $C_{L_{\dot{x}}}$ are matrices containing the lift stability and control derivatives for each strip. Note that the control input u does not contribute directly to the drag, since it is composed entirely of control commands that drive the torque motors.

After computation using the full-order model, a reduced-order form of the lift coefficient derivative matrices can be obtained in the same manner as the reduced-order output matrix is calculated in Eq. (20).

Using Eq. (26), the term $C_{L_{\dot{x}}} \dot{x}$ can be rewritten as follows:

$$C_{L_{\dot{x}}} \dot{x} = C_{L_{\dot{x}}} \left(Ax + Bu + z\right) \tag{30}$$

The control input u and the angle of attack command vector z appear in the differential equations for the torque motor states and the integral error state, respectively. Since the derivatives of these states do not contribute to the lift coefficient

$$\frac{\partial \left(C_{L_{\dot{x}}} \dot{x}\right)}{\partial u} = \frac{\partial \left(C_{L_{\dot{x}}} \dot{x}\right)}{\partial z} = 0 \tag{31}$$

and thus

$$C_{L_{\dot{x}}} \dot{x} = C_{L_{\dot{x}}} A x \tag{32}$$

It should be noted that by Eq. (7), the torque states, as opposed to their derivatives, do actually contribute to the lift force, because of the unsteady lift due to the control surface deflection acceleration $\ddot{\delta}$.

By defining

$$\bar{C}_{L_x} = C_{L_x} + C_{L_{\dot{x}}} A \tag{33}$$

the drag polar model can be rewritten as

$$C_D = C_{D_0} + \left(C_{L_0} + \bar{C}_{L_x} x\right)^\top K \left(C_{L_0} + \bar{C}_{L_x} x\right) = C_{D_0} + C_{L_0}^\top K C_{L_0} + \Delta C_D \tag{34}$$

where

$$\Delta C_D = C_{D_x} x + x^\top C_{D_{x^2}} x \tag{35}$$

and

$$C_{D_x} = 2 C_{L_0}^\top K \bar{C}_{L_x} \tag{36}$$

$$C_{D_{x^2}} = \bar{C}_{L_x}^\top K \bar{C}_{L_x} \tag{37}$$

The matrix $C_{D_{x^2}}$ is positive-definite, since K is positive-definite.

The cost function can now be expressed as

$$J = \frac{1}{2}\int_0^{t_f} \left(x^\top Q x + u^\top R u + q_D C_{D_x} x + q_D x^\top C_{D_{x^2}} x \right) dt \tag{38}$$

where $Q = Q_r \oplus Q_e \oplus Q_f \oplus Q_a > 0$.

The Hamiltonian function of the optimal control problem is defined as

$$H = \frac{1}{2}\left(x^\top Qx + u^\top Ru + q_D C_{D_x} x + q_D x^\top C_{D_{x^2}} x\right) + \lambda^\top (Ax + Bu + z) \tag{39}$$

where λ is the adjoint vector.

The adjoint equation is obtained as

$$\dot{\lambda} = -\frac{\partial H^\top}{\partial x} = -Qx - \frac{1}{2} q_D C_{D_x}^\top - q_D C_{D_{x^2}} x - A^\top \lambda \tag{40}$$

The optimality condition is

$$\frac{\partial H^\top}{\partial u} = 0 = Ru + B^\top \lambda \tag{41}$$

Solving for the optimal control yields

$$u = -R^{-1} B^\top \lambda \tag{42}$$

To solve for these equations, the adjoint equation and the state equation must be solved simultaneously along with the optimal control. Let $\lambda = Px + Sz + \lambda_0$ be a solution of the adjoint vector. Then, the adjoint equation is obtained as

$$\dot{P}x + P\dot{x} + \dot{S}z + S\dot{z} = -\left(Q + q_D C_{D_{x^2}} + A^\top P\right) x - A^\top Sz - \frac{1}{2} q_D C_{D_x}^\top - A^\top \lambda_0 \tag{43}$$

Let γ_c be a step input so that $\dot{\gamma}_c = 0$. Let $t_f \to \infty$, then the optimal solution approaches a steady state solution. Therefore, $\dot{P}(0) = 0$ and $\dot{S}(0) = 0$. Then, separating terms yields the following expressions

$$PA + A^\top P - PBR^{-1} B^\top P + Q + q_D C_{D_{x^2}} = 0 \tag{44}$$

$$S = \left(PBR^{-1} B^\top - A^\top\right)^{-1} P \tag{45}$$

$$\lambda_0 = \left(PBR^{-1} B^\top - A^\top\right)^{-1} \left(\frac{1}{2} q_D C_{D_x}^\top\right) \tag{46}$$

Equation (44) is a Ricatti equation which can be recast in a standard form as

$$PA + A^\top P - PBR^{-1} B^\top P + \bar{Q} = 0 \tag{47}$$

where

$$\bar{Q} = Q + q_D C_{D_{x^2}} \tag{48}$$

It is known that $\bar{Q} > 0$, since $Q > 0$, $q_D > 0$, and $C_{D_{x^2}} > 0$.

The optimal control is then given by

$$u = K_x x + K_z z + \Lambda_0 \tag{49}$$

where

$$K_x = -R^{-1} B^\top P \tag{50}$$

$$K_z = -R^{-1} B^\top S \tag{51}$$

$$\Lambda_0 = -R^{-1} B^\top \lambda_0 \tag{52}$$

Especially noteworthy is the term Λ_0, which unlike the two other terms is non-zero even if $x = 0$ and $z = 0$. The term Λ_0 exists due to the linear drag term $q_D C_{D_x} x$ in the cost function and enables the controller to trim the aircraft to the minimum drag trim condition using the elevator and VCCTEF.

It should be noted that in a previous study a drag-cognizant multi-objective flight control formulation has been developed for a drag model that is explicitly dependent on the control vector u. This model is essentially a quasi-steady aerodynamic model that neglects the dynamics of the flap deflections such as the deflection rate $\dot{\delta}$ and $\ddot{\delta}$.[13] Simulations of this method shows the effectiveness of the drag-cognizant multi-objective flight control.[14]

A multi-objective flight controller may be able to effectively track an angle of attack command and suppress aeroelastic modes, while reducing drag. It thereby meets its objectives. However, especially in the context of flexible aircraft, correspondence between the angle of attack and lift coefficient is not one-to-one, i.e. depending on aircraft and control state a certain angle of attack command can lead to different lift coefficient values. For example, it is

possible for a flexible aircraft to have two different lift coefficients for a given angle of attack at two different altitudes. Consequently, a multi-objective flight controller for an angle of attack command may reduce drag by reducing lift. This behavior was indeed observed in simulations of such a controller. The decrease in lift causes a decreasing flight path angle leading to loss of altitude.

In the present study, a multi-objective flight controller for a flight path angle command is implemented. A constant flight path angle corresponds to a constant lift value, hence in this context minimization of drag is equivalent to maximization of the lift-to-drag ratio, which is a common measure of aerodynamic efficiency. Additionally, a flight path angle controller has many practical applications in basic auto-pilot systems, such as altitude hold and climb rate control.

E. Sensing and State Estimation

Generally, the aeroelastic state vectors are not accessible, but can be estimated by an observer design, which is a standard control practice. It is possible to reconstruct the aeroelastic deflections from limited sensor measurements by a model-based approach. Assuming that the aeroelastic states can be reconstructed by an observer design for feedback control and that the estimation error is sufficiently small, a flight control task can be designed with the estimated aeroelastic states as feedback state variables.

It is assumed that the rigid-body and flap states are available. Consequently, the estimation problem only concerns the elastic states. The linear quadratic gaussian (LQG) is a standard technique for control design of systems with output or partial state information. A state observer is constructed using the Kalman filter optimal estimation method.

The Kalman filter receives measurements from eight accelerometers. These vertically oriented accelerometers are placed in pairs at mid-span and the wing tips. At each location, one accelerometer is placed in front of the elastic axis and one is placed behind the elastic axis. The accelerometer locations on the left wing are indicated by the four red dots in Fig. 11. By placing accelerometers in pairs it is possible to not only measure vertical acceleration of the wing section, but also angular acceleration, i.e. twist acceleration. Care must be exercised in the accelerometer signal conditioning to enable synchronous sampling to prevent phase shift among the accelerometer signals which could affect the control objective.

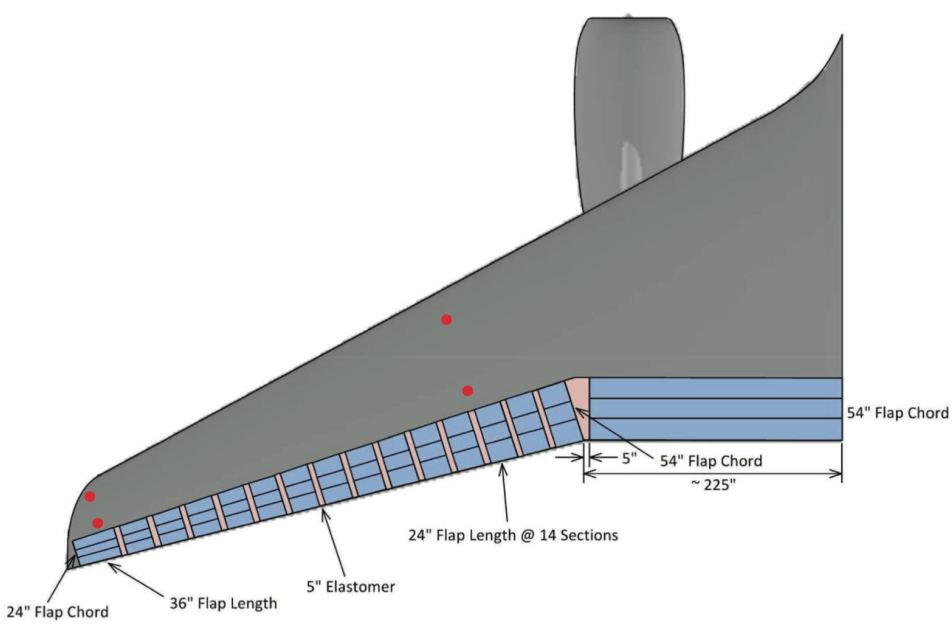

Fig. 11 - ESAC Wing with Accelerometers and VCCTEF

Before the accelerometer measurements can be used in the Kalman filter they need to pass through a low-pass filter. There are two reasons why this is necessary. Firstly, measurement noise is to be filtered out. Secondly, contributions of high frequency modes that are not maintained in the reduced-order model may negatively affect the state estimation. While these high frequency modes do not reach large deflections, they do contribute significantly to the accelerometer output, which leads to a mismatch between the measured output and the predicted output of the reduced-order model that is used to design the Kalman filter. Hence, the cut-off frequency of the low-pass filter should be chosen with the

maximum frequency of the elastic modes in the reduced-order model in mind. In order to minimize the delay of the measurement signal by limiting the phase lag of the low-pass filter, a Bessel filter is used.

Let $\hat{x}_e = \begin{bmatrix} \hat{\eta} & \dot{\hat{\eta}} & \hat{y}_\eta & \hat{z}_\eta \end{bmatrix}^\top$ be the estimation of the elastic state based on the reduced-order model. The estimation equation is then given by

$$\dot{\hat{x}}_e = A_e\hat{x}_e + +A_{er}x_r + A_{ef}x_f + L(y-\hat{y}) \tag{53}$$

where L is the well-known Kalman filter gain, x_r and x_f are the known rigid-body and VCCTEF states, and $\hat{y}$ is the estimated output

$$\hat{y} = C_r x_r + C_e\hat{x}_e + C_f x_f \tag{54}$$

It should be noted that all dynamics and output matrices in Eqs. (53) and (54) are based on the reduced-order model, as is the rest of the Kalman filter and LQR control. Also, the estimated output vector does not contain the command vector u since this term does not influence the accelerometer outputs.

The measurement output is given by

$$y = F(s)(Cx+v) \tag{55}$$

where $F(s)$ is the filter transfer function of the low-pass filter and v is the measurement noise with

$$E\left[v(t)\,v^\top(\tau)\right] = Q_v\delta(t-\tau) \tag{56}$$

where $Q_v > 0$.

In the implementation, two filter designs based on Butterworth and Bessel filters are considered. The Butterworth filter has a linear phase shift with frequency, where as the Bessel filter has a constant phase shift. It is found that the Bessel filter design performs better than the Butterworth filter in the control implementation.

The noise covariance matrix is set based on realistic noise values for the accelerometers. In Eq. (55), x represents the true state vector. The true dynamics are simulated using the nonlinear flight dynamic and full-order ASE state-space model, but for controller and observer design the linear reduced-order augmented plant of Eq. (26) is used. For the control design, additive white process noise w with

$$E\left[w(t)\,w^\top(\tau)\right] = Q_w\delta(t-\tau)$$

is included, where $Q_w > 0$ is assumed to model the effects of atmospheric turbulence and gusts and to account for discrepancies between the control and simulation models.

The drag-cognizant LQG control can be implemented using the state observer model as

$$u = K_r x_r + K_e\hat{x}_e + K_f x_f + K_z z + \Lambda_0 \tag{57}$$

where K_r, K_e, and K_f are partitioned matrices of K_x.

IV. Real-Time Drag Minimization

Multi-objective flight control can potentially enable a more functional flight control system to take advantages of multiple control surfaces available like the VCCTEF. The benefits of these flaps are driven by the aerodynamic performance objective such as drag minimization. By including a drag minimization objective in the control design, this directly addresses the ultimate goal of the PAAW technology. While this study addresses the inner-loop fast-acting control using the outermost flap segments of the VCCTEF, a more important aspect of multi-objective flight control requirement to truly achieve PAAW technology deals with the outer-loop guidance law for drag minimization during cruise. The two inner flap segments which are driven by lightweight slow-acting SMA actuators are designed to provide adaptive wing shapes during cruise that minimizes drag. This outer-loop guidance can be based on a pre-programmed schedule of flap settings based on aircraft gross weight and flight conditions. Off-line optimization can be used to define these flap settings.[7]

A more novel approach to achieving a true adaptive wing is to have the ability to determine the flap settings in real-time based on the current aircraft information. This real-time drag minimization control strategy can increase the potential benefits of PAAW technology like the VCCTEF. However, drag minimization control can be challenging in many aspects. First of all, drag sensors must be available for real-time drag minimization control. A previous study conducted by NASA Armtrong Flight Research Center has developed a peak-seeking optimization for minimizing the

fuel flow as an indication of drag.[15] Test flight on NASA F/A-18 research aircraft, tail number 853, indicates fuel flow reduction is achieved with this method. Since drag penalty is directly related to the wing shape which changes continuously in-flight at off-design flight control, it may be possible to infer drag from a wing shape sensor such as the fiber optic shape sensor (FOSS) being developed at NASA Armtrong Flight Research Center. This sensor approach will be investigated in the future.

In terms of real-time drag minimization control, performance seeking control methods can be used for real-time drag minimization.[16] A proposed real-time drag minimization control is proposed herein.

For steady-state cruise flight, the dynamics of aircraft, flexible wing, and flaps are no longer considered important, so that the drag coefficient can be expressed as

$$C_D = C_{D_0} + \left(C_{L_0} + C_{L_x}x + C_{L_u}u\right)^\top K \left(C_{L_0} + C_{L_x}x + C_{L_u}u\right) \tag{58}$$

It should be noted that u is no longer a command vector, but is a control vector such as elevator deflection δ_e, thrust δ_T, and all the VCCTEF flaps. It is also noted that the drag polar parameter K is usually not known precisely. For that matter, the lift derivatives are also not known precisely. Thus, one aspect of real-time drag minimization is parameter estimation. Let $\hat{C}_D$ be the estimate of C_D. The drag coefficient can be re-written as

$$C_D = \Theta^\top \Phi(x,u) \tag{59}$$

where $\Theta = \begin{bmatrix} C_{D_0} + C_{L_0}^\top K C_{L_0} & C_{L_0} K C_{L_x} & C_{L_0} K C_{L_u} & C_{D_{x^2}} & C_{D_{xu}} & C_{D_{u^2}} \end{bmatrix}^\top$ and
$\Phi = \begin{bmatrix} 1 & x^\top & u^\top & ele\left(xx^\top\right) & ele\left(xu^\top\right) & ele\left(uu^\top\right) \end{bmatrix}^\top$ where $ele(A)$ is the element-wise column vector of A.

Let $\hat{\Theta}$ be the estimate of Θ, $\tilde{\Theta} = \hat{\Theta} - \Theta$ be the estimation error of Θ, and $\tilde{C}_D = \hat{C}_D - C_D$ be the estimation error of C_D. Then we write

$$\tilde{C}_D = \hat{\Theta}^\top \Phi(x,u) - C_D \tag{60}$$

We seek to minimize the estimation error of C_D with the following cost function

$$J\left(\hat{\Theta}\right) = \frac{1}{2}\tilde{C}_D^2 \tag{61}$$

The gradient of the cost function with respect to $\hat{\Theta}$ is given by

$$\frac{\partial J^\top}{\partial \hat{\Theta}^\top} = \nabla J_{\hat{\Theta}}\left(\hat{\Theta}\right) = \left(\frac{\partial \tilde{C}_D}{\partial \hat{\Theta}^\top}\right)\varepsilon^\top = \Phi(x,u)\tilde{C}_D \tag{62}$$

Assuming C_D^2 is locally convex with respect to x and u. If $f \in \mathscr{C}^1$, i.e., f is differentiable at least once, then

$$f(y) \geq f(x) + \left(\nabla f(x)\right)^\top (y - x) \tag{63}$$

Furthermore, if $f \in \mathscr{C}^2$, then f is convex if $\nabla^2 f \geq 0$ where $\nabla^2 f$ is the Hessian of f.
Now consider the minimization of $J\left(\hat{\Theta}\right)$. Θ^* is said to be a global minimum of J if

$$J\left(\hat{\Theta}^*\right) \leq J\left(\hat{\Theta}\right) \tag{64}$$

This implies that $\nabla J_\Theta\left(\hat{\Theta}^*\right) = 0$ and $\nabla^2 J_{\hat{\Theta}}\left(\hat{\Theta}^*\right) \geq 0$ since $J\left(\hat{\Theta}\right)$ is twice-differentiable with respect to $\hat{\Theta}$.
Utilizing Taylor's series expansion, one writes

$$\nabla J_{\hat{\Theta}}\left(\hat{\Theta}^*\right) = \nabla J_{\hat{\Theta}}\left(\hat{\Theta}^* + \Delta\hat{\Theta}\right) + \nabla^2 J_{\hat{\Theta}}\left(\hat{\Theta}^* + \Delta\hat{\Theta}\right)\Delta\hat{\Theta} + \underbrace{\mathscr{O}\left(\Delta\hat{\Theta}^\top \Delta\hat{\Theta}\right)}_{\approx 0} \tag{65}$$

Since $\nabla J_{\hat{\Theta}}\left(\hat{\Theta}^*\right) = 0$, $\nabla J_{\hat{\Theta}}\left(\hat{\Theta}^* + \Delta\hat{\Theta}\right) = \nabla J_{\hat{\Theta}}\left(\hat{\Theta}\right)$, and $\nabla^2 J_{\hat{\Theta}}\left(\hat{\Theta}^* + \Delta\hat{\Theta}\right) = \nabla^2 J_{\hat{\Theta}}\left(\hat{\Theta}\right)$, then

$$\Delta\hat{\Theta} = -\left[\nabla^2 J_{\hat{\Theta}}\left(\hat{\Theta}\right)\right]^{-1} \nabla J_{\hat{\Theta}}\left(\hat{\Theta}\right) \tag{66}$$

Equation (66) can be written in discrete-time form as

$$\hat{\Theta}_{i+1} = \hat{\Theta}_i - \left[\nabla^2 J_{\hat{\Theta}}\left(\hat{\Theta}_i\right)\right]^{-1} \nabla J_{\hat{\Theta}}\left(\hat{\Theta}_i\right) \tag{67}$$

This is known as a second-order gradient or Newton's method for convex optimization. This approximation leads to the well-known steepest descent or first-order gradient method in discrete time

$$\hat{\Theta}_{i+1} = \hat{\Theta}_i - \varepsilon \nabla J_{\hat{\Theta}}\left(\hat{\Theta}_i\right) = \hat{\Theta}_i - \varepsilon \Phi\left(x,u\right)\left[\Phi^\top\left(x,u\right)\hat{\Theta} - C_D\right] \tag{68}$$

where $\varepsilon > 0$ is a step size, or continuous time

$$\dot{\hat{\Theta}} = -\Gamma \nabla J_{\hat{\Theta}}\left(\hat{\Theta}\right) = -\Gamma \Phi\left(x,u\right)\left[\Phi^\top\left(x,u\right)\hat{\Theta} - C_D\right] \tag{69}$$

where $\Gamma > 0$ is a learning rate.

Note that during flight operation, an aircraft passes through many different flight states. Information on drag, aircraft states, and control can be collected in flight computers for post-processing. These past data can be used to estimate drag in a least-squares sense. As more data become available, and assuming that the drag measurements are sufficiently reliable and accurate, then the least squares estimation should yield a good approximation of the drag model. Using this drag model, the control flaps can be computed for real-time drag minimization. This is done as follows:

Consider a drag minimization cost function

$$J\left(u\right) = \hat{C}_D = \hat{\Theta}^\top \Phi\left(x,u\right) \tag{70}$$

The gradient of the cost function with respect to u is given by

$$\frac{\partial J^\top}{\partial u^\top} = \nabla J_u\left(u\right) = \frac{\partial \Phi^\top\left(x,u\right)}{\partial u^\top}\hat{\Theta} \tag{71}$$

Then the control can be computed in real-time using the adaptive law

$$\dot{u} = -\Gamma \nabla J_u\left(u\right) = -\Gamma \frac{\partial \Phi^\top\left(x,u\right)}{\partial u^\top}\hat{\Theta} \tag{72}$$

Alternatively, we can write the drag model as

$$\hat{C}_D = \hat{C}_{D_0} + \hat{C}_{D_x}^\top x + \hat{C}_{D_u}^\top u + x^\top \hat{C}_{D_{x^2}} x + x^\top \hat{C}_{D_{xu}} u + u^\top \hat{C}_{D_{u^2}} u \tag{73}$$

Minimizing $\hat{C}_D$ with respect to u simply yields

$$\frac{\partial \hat{C}_D}{\partial u} = \hat{C}_{D_u} + \hat{C}_{D_{xu}}^\top x + 2\hat{C}_{D_{u^2}} u = 0 \tag{74}$$

$$u = -\frac{1}{2}\hat{C}_{D_{u^2}}^{-1}\left(\hat{C}_{D_u} + \hat{C}_{D_{xu}}^\top x\right) \tag{75}$$

However the problem with this approach could lie in the matrix inversion of $\hat{C}_{D_{u^2}}$. This matrix could be small. So when it is inverted, a large control solution may result. So, an adaptive algorithm could be used instead

$$\dot{u} = -\Gamma\left(\hat{C}_{D_u} + \hat{C}_{D_{xu}}^\top x + 2\hat{C}_{D_{u^2}} u\right) \tag{76}$$

It should be noted that the full state information may not be available such as the elastic states. Therefore, a Kalman filter will have to be designed for state estimation in conjunction with real-time drag minimization control.

We have outlined one possible real-time drag minimization strategy. There are others that could be investigated in the future. In future work, we will develop a simulation model of real-time drag minimization control to assess the feasibility of incorporating such a strategy in the PAAW technology development.

V. Simulation Results

Numerical simulations were performed to assess the performance of the multi-objective flight controller described in Section III. The simulations were run using a coupled nonlinear 6-DOF flight dynamic and full-order ASE model. The full-order model includes in total 198 symmetric and anti-symmetric elastic modes. The unsteady aerodynamics of the elastic wing and the VCCTEF are approximated using a second-order approximation of the Theodorsen's function.

The total number of states in this model is 1463. The nonlinear flight dynamic equations are integrated using a Runge-Kutta 4th-order scheme and the linear ASE state-space equations are integrated using a Newmark-β scheme. All simulations were initialized in trimmed cruise condition at 36,000 ft altitude and Mach 0.797. The initial trim was achieved using the elevator and zero VCCTEF deflection.

The following three controllers are evaluated:

- C_1 is a baseline LQR controller for tracking of a flight path angle command. It is created using a linear rigid-body model of the ESAC and VCCTEF. Since state feedback is available for the rigid-body and VCCTEF states, controller C_1 does not require the use of a Kalman filter. This controller is not aimed at aeroelastic mode suppression or minimizing drag, i.e. $q_D = 0$.

- C_2 is an LQG controller for tracking of a flight path angle command and aeroelastic mode suppression. It is created using a linear reduced-order ASE state-space model of the ESAC and VCCTEF. The control model has 10 elastic states and uses a first-order approximation of the Theodorsen's function for modeling unsteady aerodynamics. This leads to a Kalman filter with 40 state variables; 20 generalized modal coordinates and 20 aerodynamic lag states. This controller is not aimed at minimizing drag, i.e. $q_D = 0$.

- C_3 is an LQG controller for tracking of a flight path angle command, aeroelastic mode suppression, and drag minimization. It is created using the same linear reduced-order ASE state-space model of the ESAC and VCCTEF as used for controller C_2 and has the same Kalman filter state. Controller C_3 is the only controller that aims to minimize drag, i.e. $q_D > 0$.

Controllers that are designed using a rigid-body model, such as controller C_1, may have diminished performance and can even become unstable in an aeroelastic simulation model. It is found that the strong coupling between the VCCTEF and the elastic wing modes can lead to severe excitation of these modes and ultimately structural failure, if not taken into account in the controller design. This demonstrates the need for coupled flight dynamic and aeroelastic modeling of flexible vehicles.

The large variety in state variables makes the tuning of the controllers an involved process. The performance shown in this section is achieved using controllers that were iteratively tuned using the step responses of their respective reduced-order models. Controller tuning using an optimization algorithm may lead to improved results.

It is found that the tuning of controller C_1 is particularly challenging due to the large discrepancy between the controller and simulation models. Controllers that perform well on the rigid-body model may become unstable on the aeroelastic simulation model. It is found that the strong coupling between the VCCTEF and the elastic wing modes can lead to severe excitation of these modes and ultimately structural failure, if not taken into account in the controller design. This demonstrates the need for coupled flight dynamic and aeroelastic modeling of flexible vehicles.

The controllers are given a flight path angle command input, as shown in Fig. 12. After the controller is engaged at $t = 0$ sec, the aircraft performs a climb at $\gamma = 1^\circ$ (approximately 110 ft per nautical mile) and subsequently levels off. The altitude change in response to the flight path angle command is shown in Fig. 13.

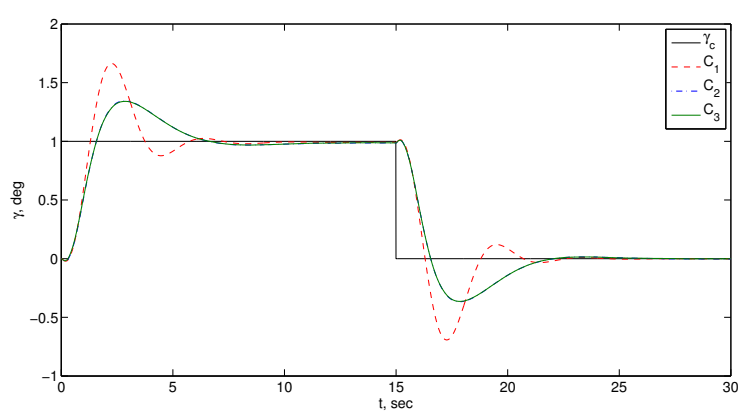

Fig. 12 - Flight Path Angle Command and Responses

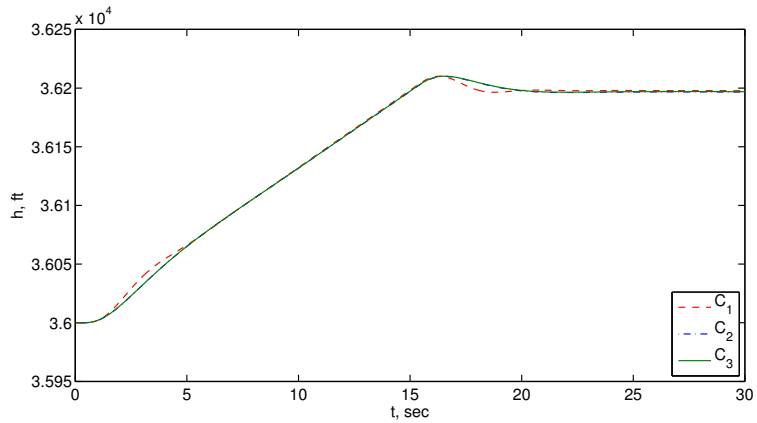

Fig. 13 - Altitude Responses to Flight Path Angle Command

The three controllers are designed to have similar tracking performance, so that comparison can focus on the other objectives. Figure 12 also shows the flight path angle response using the three controllers. It can be seen that the response of controller C_1 is initially faster than the responses of the other two controllers. However, the response subsequently shows a large overshoot and some sustained oscillations about the commanded flight path angle, leading to a similar settling time as the responses of controllers C_2 and C_3. The latter two controllers have quite similar responses.

The corresponding pitch rate responses are shown in Fig. 14. In particular, in the response corresponding to controller C_1, coupling between flight dynamic and aeroelastic modes is clearly visible. This demonstrates that a controller designed using a rigid-body model is not effective in suppressing elastic modes. The responses of controllers C_2 and C_3 are similar.

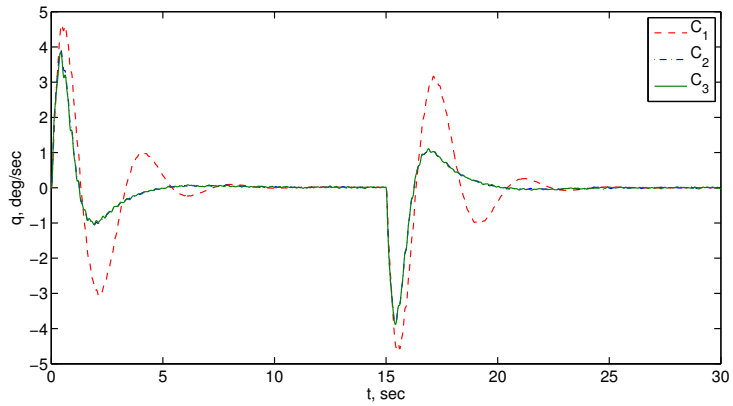

Fig. 14 - Pitch Rate Responses to Flight Path Angle Command

Examining the modal excitation of the first three symmetric modes in Figs. 15, 16, and 17, it can indeed be seen that the modal excitation is larger for controller C_1. Controllers C_2 and C_3 are more capable of damping out the aeroelastic modes.

The first symmetric mode is the first bending mode and positive excitation corresponds to upward tip deflection. It should be noted that due to the static aeroelastic deformation of the wing in trim condition, the total vertical tip deflection is upward throughout the simulation for all controllers.

The responses corresponding to controllers C_2 and C_3 are similar for the first two modes. The third symmetric mode is the first torsion mode. The response corresponding to controller C_3 shows a negative excitation, which corresponds to nose-down twist of the wing in steady-state climb and level flight.

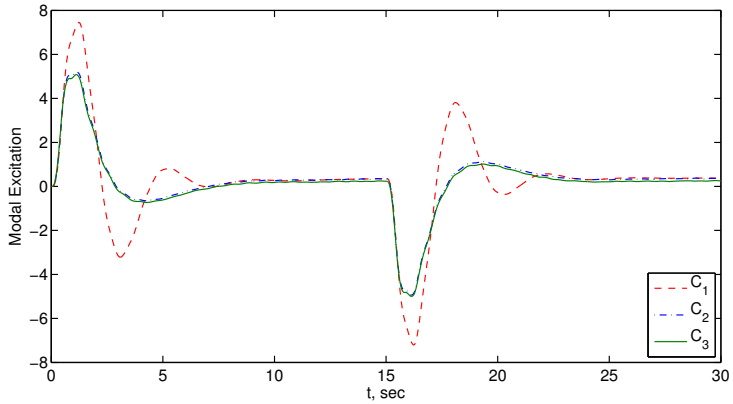

Fig. 15 - Response of First Symmetric Mode to Flight Path Angle Command

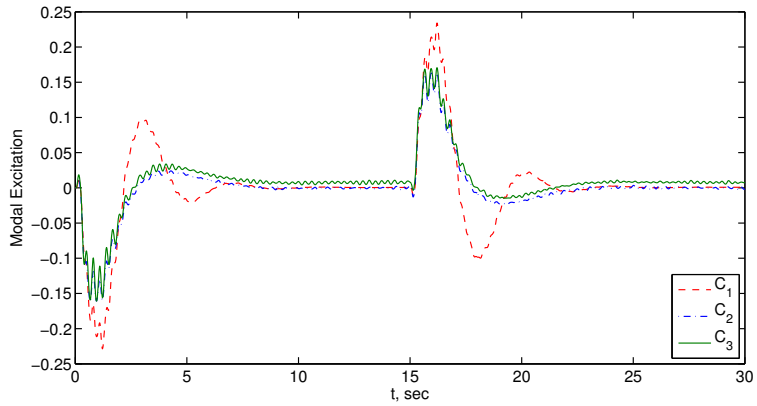

Fig. 16 - Response of Second Symmetric Mode to Flight Path Angle Command

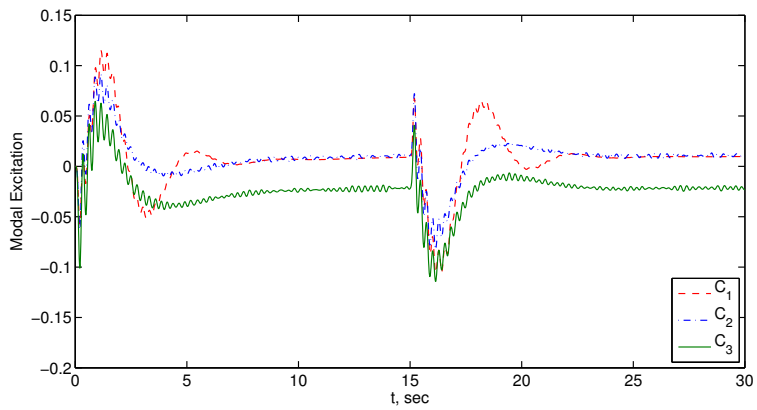

Fig. 17 - Response of Third Symmetric Mode to Flight Path Angle Command

Figures 18, 19, and 20 show the elevator and VCCTEF deflections. The control surface deflections are in the same order of magnitude for all controllers. In Fig. 20, it can be seen that for controller C_3 the VCCTEF has a steady-state deflection of about 0.5° during climb and subsequent level flight. The corresponding moment causes the nose-down twist of the wing that can be observed in Fig. 17.

Controller C_3 trims the aircraft at a minimum C_D. The trim angle of attack at $t = 30$ sec is slightly lower for controller C_3 than for controllers C_1 and C_2 by means of the VCCTEF deflection and corresponding wing shaping.

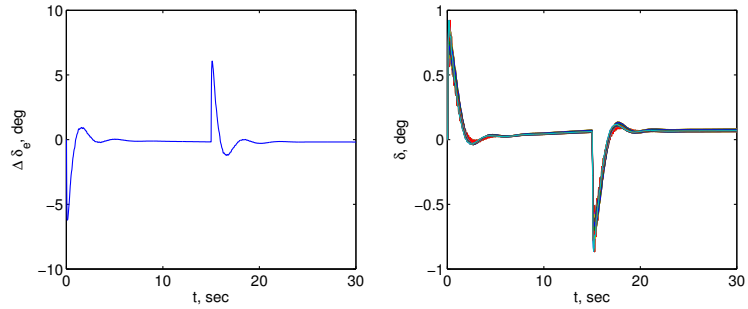

Fig. 18 - Elevator and VCCTEF Deflections for Controller C_1

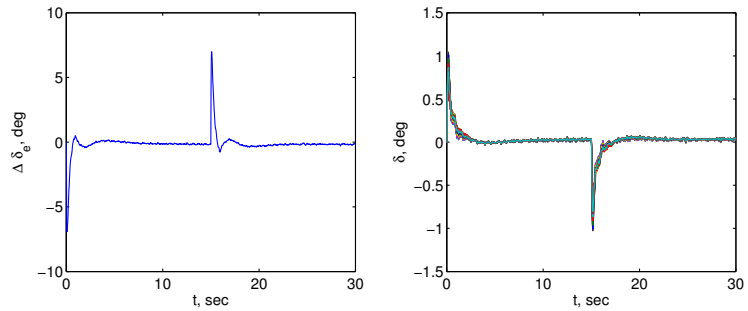

Fig. 19 - Elevator and VCCTEF Deflections for Controller C_2

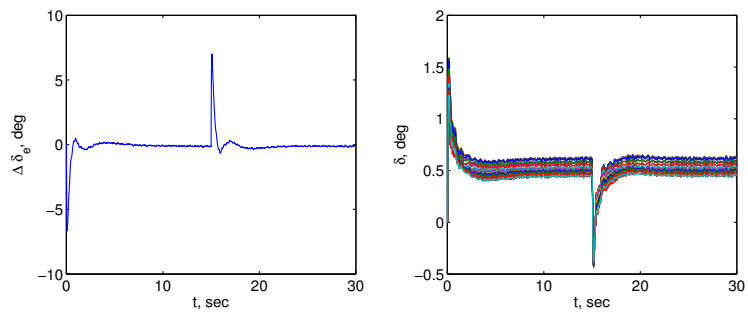

Fig. 20 - Elevator and VCCTEF Deflections for Controller C_3

It is noted that the controllers comply with the VCCTEF constraints regarding the maximum relative angle between adjacent flaps. In all three cases, the VCCTEF is controlled using four virtual commands per wing as described by Eq. (24). Without the use of virtual commands, the commands would have exceeded the VCCTEF constraints, thus causing either a saturation or an infeasible control design.

Figure 21 shows the incremental drag coefficient relative to the drag coefficient in the trim state. Due to modal excitations, the value varies more for controller C_1 than for the two other controllers. The incremental drag coefficients in trim are similar for controllers C_1 and C_2. It can be observed that the drag coefficient corresponding to the multi-objective flight controller with drag minimization, namely, controller C_3, is lower than the drag coefficient corresponding to the controllers without drag minimization.

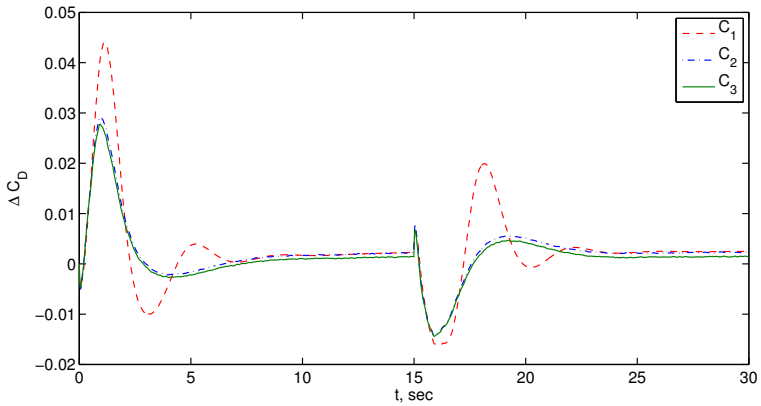

Fig. 21 - Drag Coefficient Responses to Flight Path Angle Command

The lift-to-drag ratio curves can be seen in Fig. 22. The values in the figure are normalized to the initial trim lift-to-drag ratio obtained by trimming the aircraft using the elevator without the VCCTEF deflection. During steady-state climb and level flight, controller C_3 achieves an increase in lift-to-drag ratio of approximately 4% relative to controllers C_1 and C_2.

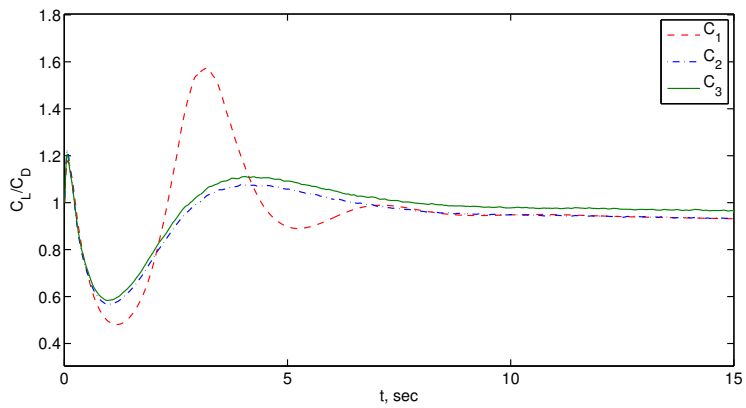

Fig. 22 - Lift-to-Drag Ratio Responses to Flight Path Angle Command

Thus, the drag minimization objective is met by controller C_3, which achieves simultaneously the flight path angle command, modal suppression, and trim solution corresponding to a minimum drag or maximum lift-to-drag ratio. The simulation results therefore demonstrate the potential benefit of the proposed multi-objective flight control design for future aircraft design with Performance Adaptive Aeroelastic Wing technology.

VI. Conclusion

A multi-objective flight control framework has been proposed to address multiple control objectives for an aircraft with Performance Adaptive Aeroelastic Wing (PAAW) technology. PAAW technology leverages multi-disciplinary solutions to maximize the aerodynamic performance payoff of future adaptive wing design, while addressing simultaneously operational constraints that can prevent the aerodynamic performance from being realized. These operational constraints include reduced aeroelastic stability margins, increased airframe responses to gust and maneuver loads, pilot handling qualities, and ride qualities. The multi-objective flight control framework addresses these issues by enabling an integrated multi-disciplinary flight control solution in order to maximize the performance benefits of PAAW technology. This is achieved by addressing simultaneously pilot command tracking tasks, aeroelastic stabilization, load alleviation, and drag minimization control design requirements. A simulation study of a multi-objective flight control for angle of attack command with aeroelastic mode suppression and drag minimization demonstrates the effectiveness of the proposed solution. The concept of virtual control is introduced to address the pair-wise flap motion

constraints imposed by the elastomer material. This method is shown to be able to satisfy the constraints. Real-time drag minimization control is considered to be an important consideration for PAAW technology. Drag minimization has many challenges such as sensing and control. An initial outline of a possible real-time drag minimization control is proposed and will be further investigated in the future.

Acknowledgment

The authors would like to thank the Fixed Wing / Advanced Air Transport Technology Project under the Fundamental Aeronautics Program of NASA Aeronautics Research Mission Directorate (ARMD) for funding support of this work. The authors also would like to acknowledge Boeing Research and Technology for their collaboration with NASA under NASA contract NNL12AD09T entitled "Development of Variable Camber Continuous Trailing Edge Flap System for B757 Configured with a More Flexible Wing."

References

[1]Nguyen, N., "Elastically Shaped Future Air Vehicle Concept," NASA Innovation Fund Award 2010 Report, October 2010, Submitted to NASA Innovative Partnerships Program, http://ntrs.nasa.gov/archive/nasa/casi.ntrs.nasa.gov/20110023698.pdf

[2]Nguyen, N., Trinh, K., Reynolds, K., Kless, J., Aftosmis, M., Urnes, J., and Ippolito, C., "Elastically Shaped Wing Optimization and Aircraft Concept for Improved Cruise Efficiency," AIAA Aerospace Sciences Meeting, AIAA-2013-0141, January 2013.

[3]Boeing Report No. 2012X0015, "Development of Variable Camber Continuous Trailing Edge Flap System," October 4, 2012.

[4]Urnes, J., Nguyen, N., Ippolito, C., Totah, J., Trinh, K., and Ting, E., "A Mission Adaptive Variable Camber Flap Control System to Optimize High Lift and Cruise Lift to Drag Ratios of Future N+3 Transport Aircraft," AIAA Aerospace Sciences Meeting, AIAA-2013-0214, January 2013.

[5]Nguyen, N, Precup, N., Urnes, J., Nelson, C., Lebofsky, S., Ting, E., and Livne, E., "Experimental Investigation of a Flexible Wing with a Variable Camber Continuous Trailing Edge Flap Design," 32nd AIAA Applied Aerodynamics Conference, AIAA-2014-2442, June 2014.

[6]Nguyen, N., Ting, E., Nguyen, D., Trinh, K., "Flutter Analysis of Mission-Adaptive Wing with Variable Camber Continuous Trailing Edge Flap," 55th AIAA/ASME/ASCE/AHS/ASC Structures, Structural Dynamics, and Materials Conference, AIAA-2014-0839, January 2014.

[7]Lebofsky, S., Ting, E., and Nguyen, N., "Aeroelastic Modeling and Drag Optimization of Flexible Wing Aircraft with Variable Camber Continuous Trailing Edge Flap," 32nd AIAA Applied Aerodynamics, AIAA 2014-2443, June 2014.

[8]Nguyen, N., Ting, E., Nguyen, D., and Trinh, K., "Flight Dynamic Modeling and Stability Analysis of Flexible Wing Generic Transport Aircraft," 55th AIAA/ASME/ASCE/AHS/ASC Structures, Structural Dynamics, and Materials Conference, AIAA-2014-1040, January 2014.

[9]Tal, E., Nguyen, N. and Ting, E., "Comparison of Unsteady Aerodynamics Approximations for Time-Domain Representation of Frequency-Independent Aeroelastic State-Space Models," 56th AIAA/ASME/ASCE/AHS/ASC Structures, Structural Dynamics, and Materials Conference, January 2015.

[10]Nguyen, N., Swei, S., and Ting, E., "Adaptive Linear Quadratic Gaussian Optimal Control Modification for Flutter Suppression of Adaptive Wing," AIAA Infotech@Aerospace Conference, AIAA 2015-0118, January 2015.

[11]Kokotovic, P., Khalil, H., and O'Reilly, J., *Singular Perturbation Methods in Control: Analysis and Design*, Society for Industrial and Applied Mathematics, 1987.

[12]Ardema, M., "Computational Singular Perturbation Method for Dynamical Systems", AIAA Journal of Guidance, Control, and Dynamics, Vol. 14, 661-663, 1981.

[13]Nguyen, N. and Urnes, J., "Aeroelastic Modeling of Elastically Shaped Aircraft Concept via Wing Shaping Control for Drag Reduction," AIAA Atmospheric Flight Mechanics Conference, AIAA-2012-4642, August 2012.

[14]Ippolito C. and Nguyen, N., "A Preliminary Study for Optimal Longitudinal-Mode Flight Control through Distributed Aeroelastic Shaping," 55th AIAA/ASME/ASCE/AHS/ASC Structures, Structural Dynamics, and Materials Conference, AIAA-2014-1044, January 2014.

[15]Brown, N. and Schaefer, J., "Peak-Seeking Optimization of Trim for Reduced Fuel Consumption: Flight-Test Results," AIAA Guidance, Navigation, and Control Conference, AIAA-2013-5171, August 2013.

[16]Nobbs, S.G., "Development of the Full-Envelope Performance Seeking Control Algorithm," 28th AIAA Joint Propulsion Conference, AIAA-1992-3748, July 1992.